Nano Research Energy

ISSN 2791-0091 (print); 2790-8119 (online)
https://doi.org/10.26599/NRE.2026.9120261

Research Article

Capture-to-catalyst hollow N-doped porous carbons for closed-loop gold recovery and nitrate-to-ammonia electrocatalysis

Yutong Ding[1,§], Ruicong Geng[1,§], Wenzhao Duan[2], Zheng-Jun Wang[2], Jing-Jing Lv[2] (✉), Ge Meng[2] (✉), Wenxian Liu[1] (✉), and Tairong Kuang[1] (✉)

[1] *Functional Polymers & Advanced Materials (FPAM) Lab, State Key Laboratory of Advanced Separation Membrane Materials, Zhejiang Key Laboratory of Advanced Polymer Materials Modification and Application Technology, College of Materials Science and Engineering, Zhejiang University of Technology, Hangzhou 310014, China*

[2] *College of Chemistry and Materials Engineering, Wenzhou University, Wenzhou 325035, China*

[§] *Yutong Ding and Ruicong Geng contributed equally to this work.*

Received: 29 June 2026 / **Revised:** 4 August 2026 / **Accepted:** 6 August 2026

ABSTRACT

Materials that recover dilute metals and convert the recovered species into functional catalysts can link resource circularity with environmental remediation, yet their design is constrained by a trade-off between rapid transport and reactive binding. Here, we report a ZIF−8-derived hollow N-doped porous carbon (HNPC) as a capture-to-catalyst platform for closed-loop gold recovery and nitrate-to-ammonia electrocatalysis. The hollow mesoporous framework shortens diffusion pathways and improves access to internal surfaces, whereas graphitic-N-associated sites promote $AuCl_4^-$ adsorption and Au(III)-to-Au(0) reduction. The optimized HNPC exhibits a Langmuir Au(III) capacity of 3245.1 mg·g^{-1} and removes >99.9% of Au at trace concentrations under strong ionic competition, corresponding to a distribution coefficient of ~3×10^9 mL·g^{-1}. Time-resolved microscopy and spectroscopy reveal rapid Au nanoparticle nucleation and progressive conversion to Au(0), while finite−element simulations and density functional theory (DFT) identify the cooperative roles of hollow-structure-enabled transport and graphitic-N-regulated interfacial reactivity. The resulting Au/HNPC is directly reused as a gas-diffusion-electrode catalyst, delivering 96.6% Faradaic efficiency for nitrate-to-ammonia conversion and stable operation for 535 h at 200 mA·cm^{-2}. This work establishes a materials strategy for integrating selective recovery, *in situ* metal formation, and catalytic reuse in complex aqueous media.

KEYWORDS

hollow N-doped porous carbon, gold recovery, reactive adsorption, capture-to-catalyst strategy, nitrate-to-ammonia electrocatalysis

1 Introduction

Materials capable of extracting dilute resources and transforming the captured species into functional components are increasingly important for closed-loop materials systems [1–7]. Gold recovery from electronic waste represents a compelling case because gold is indispensable in electronics and catalysis, whereas primary gold production remains energy-intensive and environmentally burdensome [8–10]. In practical hydrometallurgical leachates, gold is typically present as chloro-complex anions, particularly $AuCl_4^-$, at trace-to-ppm concentrations together with large excesses of competing ions across a broad acidity range [11, 12]. Efficient recovery from such complex streams requires a high-performance materials platform. This platform must integrate rapid ion transport with strong and selective target binding. Furthermore, it should enable interfacial Au(III)-to-Au(0) conversion while stabilizing the generated Au domains for downstream functional reuse.

Porous adsorbents have been widely explored for Au(III) recovery because they can preconcentrate target ions from dilute solutions and, in some cases, promote *in situ* reduction to metallic Au [13–15]. However, most reported systems remain limited by a coupled transport-reactivity trade-off. Strategies that strengthen adsorption thermodynamics typically rely on increasing the density of soft-donor or redox-active motifs, as in sulfur−rich polymers [16, 17] or heteroatom−doped carbons [18–21]. Although such chemistries can enhance the affinity toward $AuCl_4^-$ and promote reduction, they often reduce pore accessibility, slow intraparticle diffusion, and shift extraction toward a transport−limited regime, especially under strong ionic competition [22–24]. Conversely, hierarchical porosity or enlarged

Address correspondence to Tairong Kuang, kuangtr@zjut.edu.cn; Jing-Jing Lv, jjlyu@wzu.edu.cn; Wenxian Liu, liuwx@zjut.edu.cn; Ge Meng, mengge@wzu.edu.cn

transport channels can accelerate mass transport [25, 26], but may weaken the local electrostatic and electronic environment required to stabilize $AuCl_4^-$ and drive interfacial Au(III) reduction [3, 27–29]. Recent framework-based sorbents further illustrate this dilemma: MOF-based composites and functionalized covalent organic frameworks can improve binding-site density, pore accessibility, or redox activity [30–33], yet transport geometry and interfacial reactivity are still most often optimized as separate design variables [34–36]. As a result, rapid transport, efficient site utilization, strong selectivity, and reactive Au(III)-to-Au(0) conversion are rarely achieved simultaneously in leachates containing trace Au under strong ionic competition.

Beyond this capture-focused limitation, a further materials-design challenge is that recovered metals are commonly treated as terminal products rather than as functional components for downstream use. For a closed-loop recovery system, the sorbent should not only capture and reduce $AuCl_4^-$ efficiently, but also stabilize the generated Au domains in a form that can be directly reused. This requirement places simultaneous constraints on the spatial organization of transport pathways, accessible adsorption sites, redox-active heteroatom centers, and metal domains within one scaffold. A material architecture that integrates transport-accessible $AuCl_4^-$ capture, interfacial Au(III)-to-Au(0) conversion, Au domain stabilization, and downstream catalytic reuse therefore remains underdeveloped.

Here, we report a ZIF-8-derived hollow N-doped porous carbon (HNPC) as a capture-to-catalyst materials platform for closed-loop gold recovery and nitrate-to-ammonia electrocatalysis (Fig. 1(a)). Specifically, the closed-loop refers to the direct conversion of recovered e-waste gold into active electrocatalysts for nitrate-to-ammonia synthesis. HNPC is constructed through ZIF-8 templating, tannic-acid-assisted selective etching, and carbonization, producing a hollow mesoporous carbon framework enriched with graphitic N. The hollow architecture shortens diffusion pathways and exposes accessible internal surfaces, whereas graphitic-N-associated sites provide a favorable electrostatic and electronic microenvironment for $AuCl_4^-$ adsorption and Au(III)-to-Au(0) reduction. This integrated design enables high-capacity and selective Au recovery in model solutions, competitive media, and real e-waste leachates, with performance benchmarking summarized in Fig. 1(b). Mechanistic analyses integrating transport modeling, time-resolved spectroscopy, and density functional theory calculations reveal how hollow-structure-enabled diffusion and graphitic-N-regulated interfacial reactivity cooperate during Au capture-to-reduction. The Au formed *in situ* on HNPC is then directly reused as a gas-

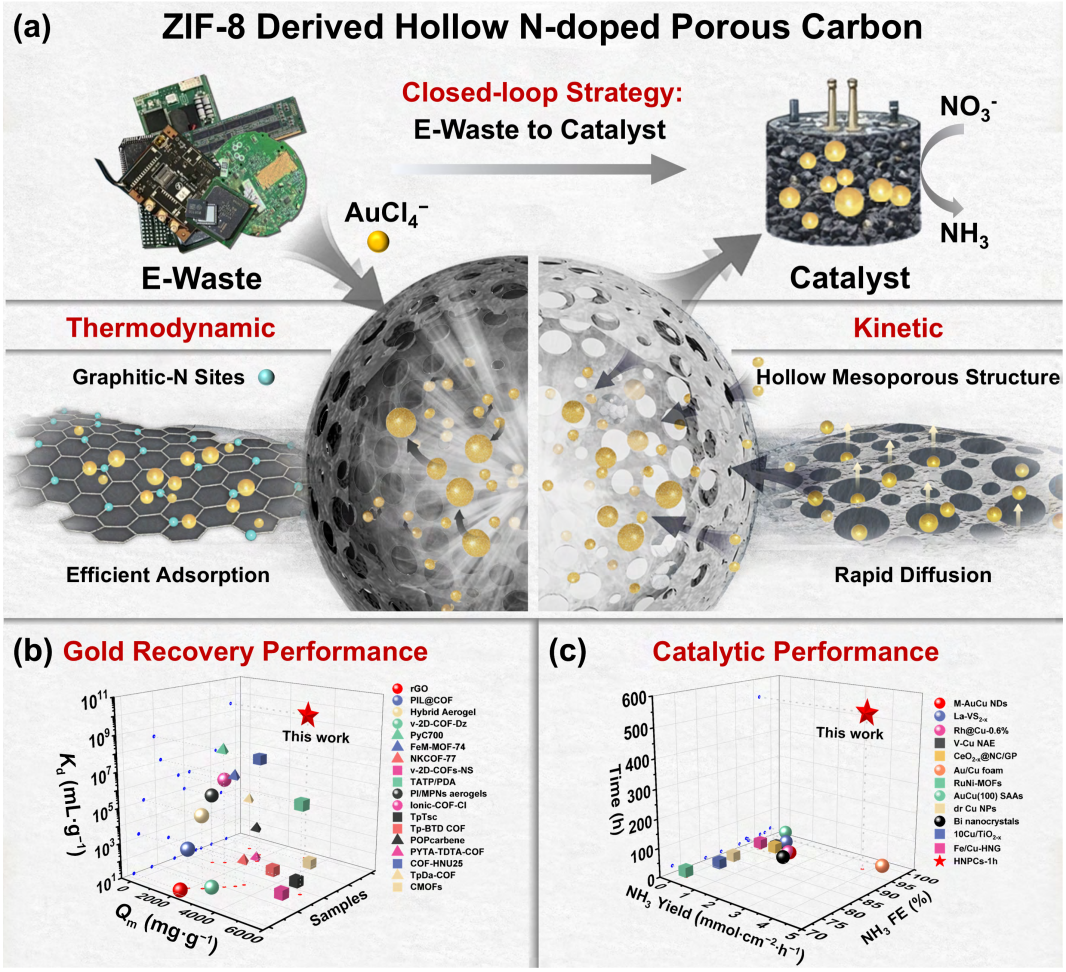

Figure 1 Closed–loop concept and performance benchmarking of HNPC for gold recovery and nitrate–to–ammonia electrosynthesis. (a) Schematic illustration of the closed–loop strategy: hollow N–doped porous carbon (HNPC) selectively captures and reduces $AuCl_4^-$ from complex e–waste leachates to form Au/HNPC, which is subsequently upcycled as an electrocatalyst for nitrate–to–ammonia conversion. (b) Comparison of the maximum Au(III) adsorption capacity (Q_m) and distribution coefficient (K_d) of this work with representative reported gold adsorbents under comparable conditions. (c) Benchmarking of representative nitrate–to–ammonia electrocatalysts in terms of NH_3 Faradaic efficiency, NH_3 yield rate, and continuous operation time, highlighting the balanced selectivity–productivity–durability profile of Au/HNPC.

diffusion-electrode catalyst for nitrate-to-ammonia conversion, with electrocatalytic benchmarking shown in Fig. 1(c). This work establishes a capture-to-catalyst materials strategy that links e-waste gold valorization with catalytic nitrate remediation.

2 Results and discussion

2.1 Construction of a hollow N-doped porous carbon platform

To implement the capture-to-catalyst materials strategy outlined in Fig. 1(a), HNPC was synthesized through a sequential templating–etching–carbonization route (Fig. S1 in the Electronic Supplementary Material (ESM)). Briefly, ZIF–8 nanocrystals were prepared from 2-methylimidazole and Zn^{2+}, selectively etched with tannic acid to generate a hollow ZIF–8 precursor (HZIF–8), and then carbonized under N_2 at 900 °C to afford the hollow carbon framework. A solid counterpart derived from pristine ZIF–8 without the etching step was prepared as a control (NPC). Scanning electron microscopy (SEM) images show that pristine ZIF–8 consists of uniform dodecahedral particles with an average size of ~200 nm (Fig. S2(a) in the ESM), whereas tannic-acid etching preserves the polyhedral shell while generating a distinct internal cavity (Fig. S2(b) in the ESM). The etched precursor retains the ZIF-8 crystal structure, as evidenced by the unchanged powder X-ray diffraction (PXRD) peak positions (Fig. S3 in the ESM). After carbonization, the characteristic ZIF–8 reflections disappear and a broad carbon (002) feature appears at ~23.5° (Fig. S4 in the ESM), consistent with conversion to turbostratic carbon. SEM and transmission electron microscopy (TEM) images further reveal that HNPC contains an internal void bounded by a thin carbon shell, whereas NPC remains densely filled and lacks an internal cavity (Figs. S5–S7 in the ESM). Elemental mapping confirms a uniform distribution of C, N, and O throughout the HNPC framework (Fig. S6 in the ESM). N_2 sorption measurements show type-IV isotherms with hysteresis for both samples (Fig. S8 in the ESM), indicating mesoporosity. Although HNPC exhibits a lower Brunauer–Emmett–Teller (BET) surface area than NPC (1026 vs. 1324 $m^2 \cdot g^{-1}$), its hollow interior and interconnected mesopores provide a structural basis for transport-efficient access to internal reactive sites during Au(III) capture [37].

2.2 Hollow architecture enables transport-accelerated Au(III) uptake

To evaluate the kinetic benefit of the hollow architecture, Au(III) adsorption on HNPC and NPC was compared under identical conditions (Fig. 2). The kinetic tests were performed at a relatively low adsorbent dosage to avoid rapid depletion of dissolved Au(III), which would otherwise obscure rate differences. Time-dependent concentration profiles show faster Au(III) depletion for HNPC than for NPC (Fig. 2(a)). Intraparticle-diffusion analysis using the Weber–Morris model [38] resolves three regimes for both samples, corresponding to external diffusion (k_{d1}), intraparticle diffusion (k_{d2}), and near–equilibrium uptake (k_{d3}) (Fig. 2(b)). HNPC exhibits larger rate constants across all three regimes (k_{d1} = 765.3, k_{d2} = 378.6, and k_{d3} = 79.9 $mg \cdot g^{-1} \cdot h^{-1/2}$) than NPC ($k_{d1}$ = 375.9, k_{d2} = 218.1, and k_{d3} = 40.8 $mg \cdot g^{-1} \cdot h^{-1/2}$) (Table S2 in the ESM), indicating faster mass transport from the external solution to the particle interior.

Kinetic fitting further supports a chemisorption-dominated uptake process. The pseudo-second-order model describes the adsorption profiles for both HNPC and NPC with high correlation coefficients (R^2 = 0.99; Fig. 2(c) and Table S3 in the ESM), whereas the pseudo-first-order model gives poorer fits (Fig. S9 and Table S3 in the ESM). For HNPC, the experimentally measured equilibrium uptake (Q_{exp} = 3973.4 $mg \cdot g^{-1}$) approaches the mass-balance limit imposed by the initial Au loading (4000 $mg \cdot g^{-1}$ under the kinetic-test conditions; see the ESM, Adsorption Kinetics), consistent with near-quantitative capture. The fitted pseudo-second-order Q_e slightly exceeds this limit because it is an extrapolated model parameter obtained under near-saturation conditions; accordingly, Q_{exp} is used for physical capacity reporting, whereas fitted Q_e is used only for kinetic comparison. Although HNPC shows a slightly smaller k_2 than NPC, its much larger Q_e leads to a substantially higher initial adsorption rate h (1857.7 vs. 397.5 $mg \cdot g^{-1} \cdot h^{-1}$) (Table S3 in the ESM), consistent with the experimentally observed acceleration of uptake [39, 40]. A summary of the kinetic descriptors further highlights the transport advantage of the hollow architecture (Fig. 2(d)).

Finite-element simulations were performed to visualize transport at the particle scale. In the simplified models, HNPC was represented as a hollow hexagonal particle and NPC as a solid hexagon with identical outer dimensions (Fig. S10 in the ESM) [41]. At early times (t = 0.1 s), the hollow model exhibits a higher diffusion flux than the solid model (Figs. 2(e) and 2(f)), indicating more efficient ingress of Au-bearing species [42]. Spatiotemporal concentration maps further show faster accumulation and higher local Au(III) concentration within the hollow geometry (Fig. 2(g)) [43]. At t = 0.5 s, the average concentration in the hollow model reaches 949.1 $mol \cdot m^{-3}$, nearly three times higher than that in the solid model (343.5 $mol \cdot m^{-3}$) (Fig. 2(h)). These simulations support the experimental kinetic results and indicate that the hollow architecture shortens effective diffusion pathways, thereby increasing the fraction of reactive sites that can be accessed under dilute and competitive conditions [44, 45].

2.3 Reactive Au capture-to-reduction on HNPC

Because Au(III) capture by N–doped carbons can be coupled with interfacial reduction, we tracked the evolution of surface Au species on HNPC using complementary microscopy and spectroscopy (Fig. 3 and Figs. S11–S14 in the ESM). TEM shows no discernible deposits on pristine HNPC, whereas small, well-dispersed nanoparticles appear after only 0.5 min of exposure to Au(III) solution, indicating rapid nucleation of metallic Au on the carbon surface (Fig. 3(a)) [46]. With longer contact times (1 h), the nanoparticle density increases and the particles grow further; after 24 h, the surface is covered by larger, partially coalesced Au domains (Fig. 3(a)). Consistently, PXRD shows the progressive appearance and strengthening of metallic Au reflections, including the peaks at 38.2° and 44.4° (Fig. S11 in the ESM).

X-ray photoelectron spectroscopy (XPS) provides direct evidence for the time-dependent Au(III)-to-Au(0) transformation. At 0.5 min, Au 4f peaks characteristic of Au(III) appear at 86.88 eV ($4f_{7/2}$) and 90.58 eV ($4f_{5/2}$), whereas prolonged adsorption leads to the growth of Au(0) peaks at 84.38 and 88.08 eV (Fig. 3(b) and Fig. S12 in the ESM) [47]. Quantitative deconvolution indicates that more than 96% of the surface Au is present as Au(0) after 24 h (Fig. 3(b)). In parallel, the graphitic-N component in the N 1s spectrum shifts from 401.4 to 402.4 eV with increasing adsorption time, while pyridinic and pyrrolic N show minor changes (Fig. S13 in the ESM), suggesting that graphitic-N-

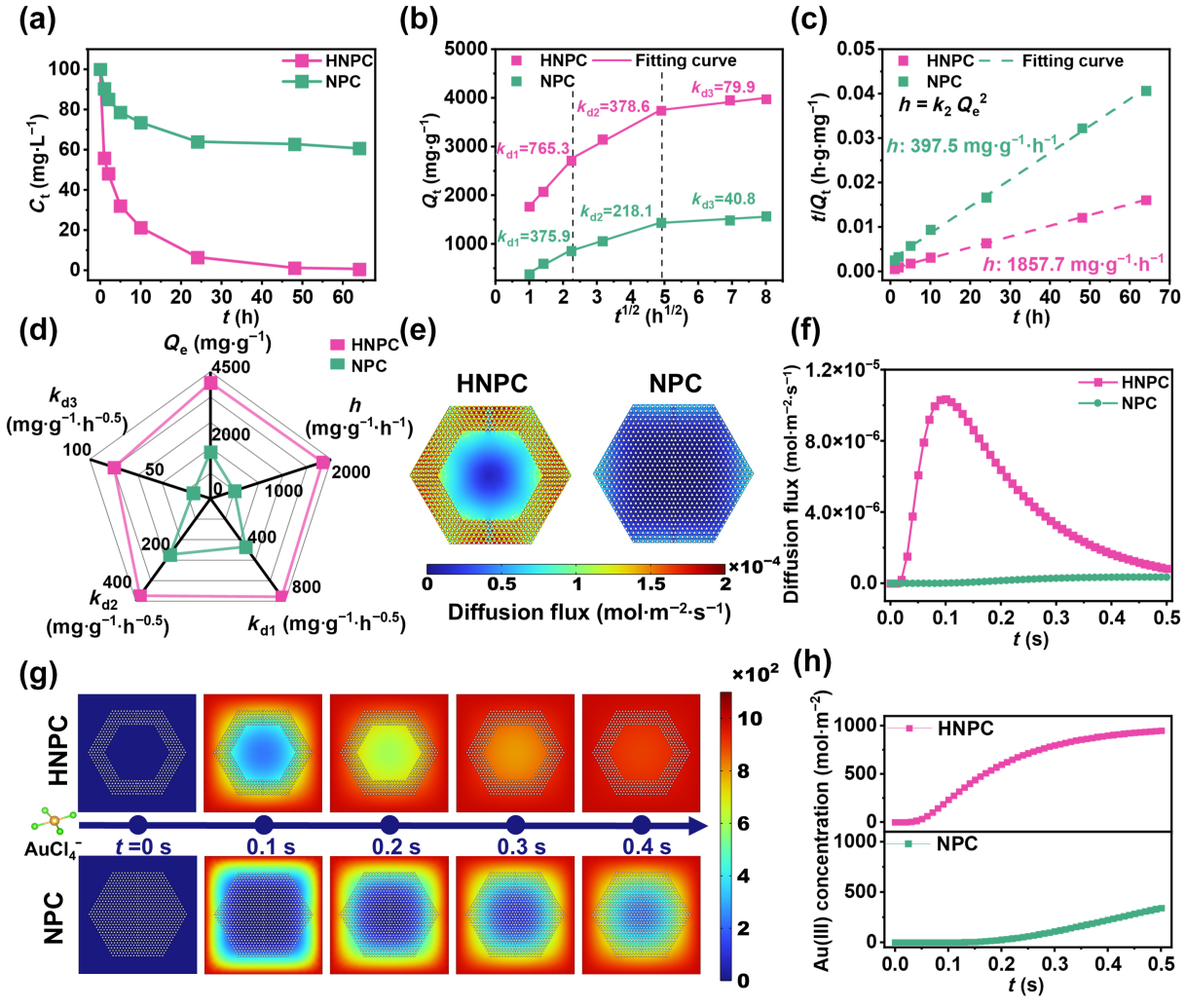

Figure 2 Hollow architecture accelerates mass transport and adsorption kinetics for Au(III) capture. (a) Time–dependent residual Au(III) concentration (C_t) during adsorption on HNPC and solid NPC. (b) Weber–Morris intraparticle diffusion plots (Q_t vs. $t^{1/2}$) with three–stage linear fitting, where k_{d1}, k_{d2}, and k_{d3} denote diffusion rate constants at the external diffusion, intraparticle diffusion, and near–equilibrium stages, respectively. (c) Pseudo–second–order (PSO) kinetic fitting plots (t/Q_t vs. t) for Au(III) adsorption on HNPC and NPC, with the calculation of initial adsorption rate (h). (d) Radar chart summarizing key kinetic descriptors (Q_e, initial adsorption rate h, and k_{d1}–k_{d3}). (e) Finite–element simulation (COMSOL) of Au species diffusion flux distributions for simplified hollow (HNPC) and solid (NPC) particle models at an early time (t = 0.1 s). (f) Simulated evolution of the overall diffusion flux as a function of time for hollow vs. solid models. (g) Time–resolved spatial concentration maps of Au species within hollow and solid models (t = 0–0.4 s), illustrating faster accumulation inside the hollow model. (h) Time–dependent averaged Au(III) concentration inside the particle models.

associated sites participate in the interfacial electron transfer that converts captured $AuCl_4^-$ into metallic Au domains [3]. Raman spectra also show a progressive increase in I_D/I_G from 0.97 to 1.03 between 0.5 min and 24 h (Fig. S14 in the ESM), consistent with local electronic perturbation of the carbon framework during the redox process [13].

Synchrotron X-ray absorption spectroscopy further resolves the coordination evolution of Au during capture and reduction. With increasing adsorption time, the Au L_3-edge XANES edge gradually shifts to lower energy and approaches that of metallic Au after 24 h (Fig. 3(c)), consistent with progressive reduction to Au(0) [48]. Fourier-transformed EXAFS spectra reveal Au-Cl coordination at ~2.26 Å at early times and Au-Au metallic bonding at ~2.85 Å (Fig. 3(d) and Table S4 in the ESM). Quantitative fitting shows that the Au-Cl coordination number decreases from 0.7 to 0, while the Au-Au coordination number increases from 7.3 to ~10 as adsorption proceeds (Table S4 in the ESM) [49]. Wavelet-transform analysis likewise shows attenuation of the Au-Cl feature ($k \approx 5.5$ Å^{-1}) and growth of the Au-Au feature ($k \approx 9$ Å^{-1}) (Fig. 3(e)) [15]. Together, these results support an interfacial electron-transfer pathway in which adsorbed $AuCl_4^-$ undergoes stepwise dechlorination and reduction on graphitic-N-regulated sites, followed by Au domain nucleation, growth, and coalescence within the hollow carbon scaffold (Fig. 3(f)).

2.4 Graphitic nitrogen regulates interfacial $AuCl_4^-$ reduction

To correlate Au(III) uptake with nitrogen speciation and carbon structure, HNPC samples were prepared at carbonization temperatures ranging from 700 to 1000 °C. Increasing the carbonization temperature sharpens the broad PXRD features and decreases the Raman I_D/I_G ratio from 1.12 at 700 °C to 0.97 at 1000 °C, indicating progressively enhanced graphitization (Figs. S15 and S16 in the ESM) [50]. Adsorption isotherms for this series are well described by the Langmuir model ($R^2 > 0.92$; Fig. 4(a) and Table S5 in the ESM), consistent with site-limited adsorption coupled with reduction [51]. The maximum Au(III) adsorption capacity exhibits a volcano-type dependence on carbonization

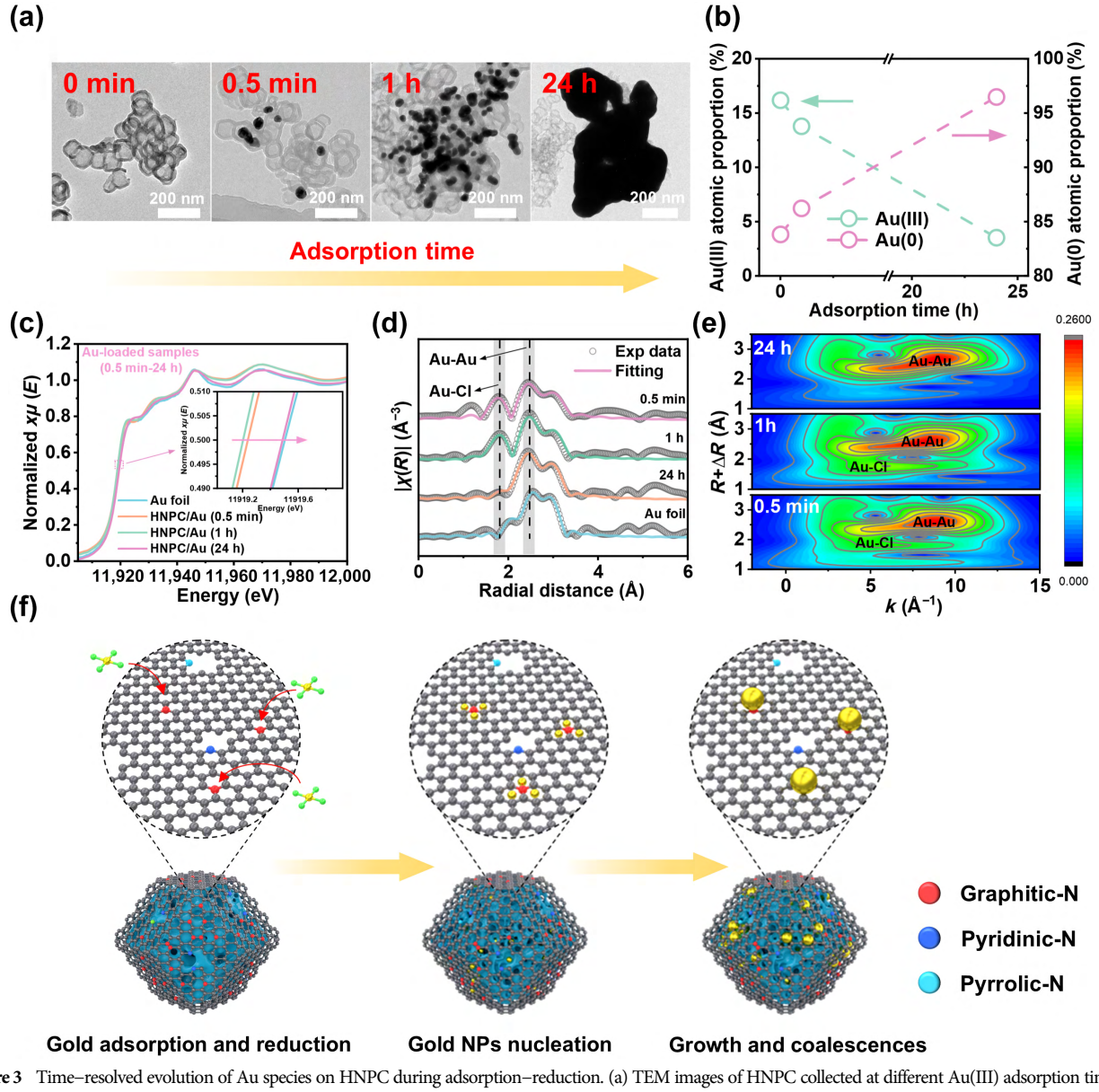

Figure 3 Time–resolved evolution of Au species on HNPC during adsorption–reduction. (a) TEM images of HNPC collected at different Au(III) adsorption times (0 min, 0.5 min, 1 h, and 24 h), showing nucleation, growth, and coalescence of reduced Au nanoparticles on HNPC (scale bars: 200 nm). (b) XPS–derived atomic proportion of Au(III) and Au(0) species as a function of adsorption time. (c) Normalized Au L_3–edge XANES spectra of Au foil and Au–loaded HNPC at different adsorption times; inset shows the edge–position shift toward metallic Au with time. (d) Fourier–transformed EXAFS ($|\chi(R)|$) and fitting results. (e) Wavelet–transform (WT) analysis of k^3–weighted EXAFS oscillations. (f) Schematic illustration of the interfacial adsorption–electron transfer–reduction pathway leading to Au nanoparticle nucleation, growth, and coalescence on HNPC.

temperature, reaching a maximum for HNPC-900 (Q_m = 3245.1 mg·g^{-1}) and decreasing at higher temperatures (Fig. 4(a)). XPS analysis shows that HNPC-900 possesses the highest graphitic-N fraction (2.14%) among the series (Fig. 4(b) and Fig. S17 in the ESM). These results indicate that carbonization temperature regulates the balance between graphitization and active-site preservation. Although higher temperatures promote graphitic structural development, excessive carbonization at 1000 °C decreases nitrogen-containing active sites and may compromise the porous architecture. In contrast, insufficient graphitization at 700 °C limits the formation of favorable electronic structures. Therefore, HNPC-900 represents an optimal balance between graphitic-N retention and structural integrity, resulting in the highest Au(III) adsorption capacity. Zeta-potential measurements reveal the most positive surface potential for HNPC-900 (28.8 mV at pH=4), followed by HNPC-800, HNPC-1000, and HNPC-700 (Fig. S18 in the ESM) [52], consistent with enhanced electrostatic attraction toward $AuCl_4^-$ species.

DFT calculations were performed to clarify the preference for graphitic-N-associated sites and to connect electronic structure with $AuCl_4^-$ stabilization and reduction (Figs. 4(c)–4(g) and Fig. S19 in the ESM) [53]. Electrostatic-potential maps show that the graphitic-N model provides a more positively polarized adsorption environment (+1.10 eV) than pyridinic-N (−1.45 eV) and pyrrolic-N (−2.12 eV) models, favoring adsorption of the anionic $AuCl_4^-$ complex (Fig. 4(c)) [54]. Adsorption energies follow the order graphitic-N (−1.52 eV) < pyridinic-N (−1.41 eV) < pyrrolic-N (−1.18 eV), indicating stronger $AuCl_4^-$ binding at graphitic-N sites (Fig. 4(d)) [55]. Mulliken charge analysis suggests more pronounced electron transfer to the Au-containing intermediate at graphitic-N sites (ΔQ = +0.07|e|) (Fig. 4(e)) [56, 57]. Frontier-orbital analysis further shows that the graphitic-

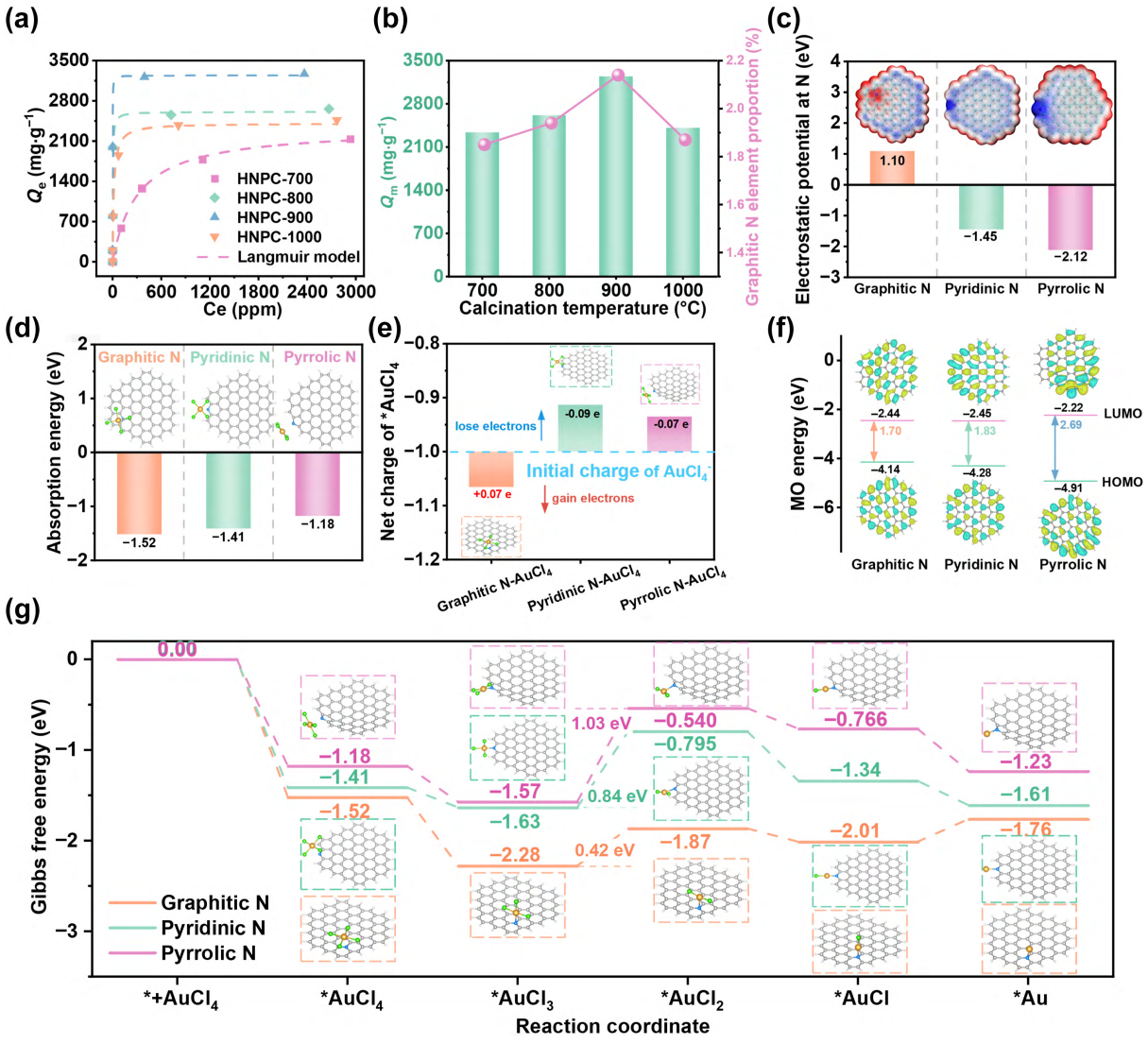

Figure 4 Graphitic-N–regulated thermodynamics and kinetics for $AuCl_4^-$ adsorption and reduction. (a) Au(III) adsorption isotherms of HNPC samples pyrolyzed at different temperatures (HNPC–700/800/900/1000) with Langmuir fitting. (b) Correlation between the Langmuir maximum adsorption capacity (Q_m) and graphitic-N proportion (from XPS) as a function of calcination temperature. (c) Calculated electrostatic potential at different N configurations (graphitic N, pyridinic N, and pyrrolic N). (d) DFT–calculated adsorption energies of $AuCl_4^-$ on different N–doped carbon models (structures shown), highlighting stronger binding on graphitic-N sites. (e) Mulliken charge analysis showing the net charge of adsorbed *$AuCl_4$ and charge transfer (ΔQ) at different N sites. (f) Frontier orbital analysis (HOMO/LUMO levels and gaps) of the different N configurations. (g) Gibbs free energy diagram for the stepwise dechlorination/reduction pathway (*$AuCl_4$→ *$AuCl_3$→ *$AuCl_2$→ *AuCl→ *Au) on Graphitic-N, Pyridinic–N, and Pyrrolic–N sites.

N model has the highest HOMO level (−4.14 eV) and the smallest HOMO-LUMO gap (1.70 eV) among the three N configurations (Fig. 4(f)), consistent with more favorable electron-donor character [58]. Free-energy calculations for stepwise dechlorination and reduction identify *$AuCl_3$→*$AuCl_2$ as the potential-determining step, with the lowest barrier on graphitic-N (ΔG_{PDS} = 0.42 eV) compared with pyridinic-N (0.84 eV) and pyrrolic-N (1.03 eV) (Fig. 4(g)) [59–61]. These calculations rationalize the experimentally observed volcano-type behavior and support graphitic N as an active motif that couples $AuCl_4^-$ adsorption, interfacial reduction, and subsequent Au domain formation.

2.5 Selective gold recovery from complex leachates

The robustness of HNPC for Au recovery was evaluated under wide pH ranges, strong ionic competition, repeated regeneration, and real e-waste leachate conditions (Fig. 5 and Figs. S20 and S21 in the ESM). HNPC maintains near-quantitative Au(III) removal (≥99%) across pH=1–11 (Fig. 5(a)), benefiting from the enhanced electrostatic attraction between protonated nitrogen sites and $AuCl_4^-$ species under acidic conditions, together with the high chemical stability of the carbon framework. In a competitive solution containing 10 ppm Au(III) and 100 ppm each of Na^+, Mg^{2+}, Ni^{2+}, Cu^{2+}, and Zn^{2+}, HNPC selectively removes >99.9% of Au(III) while exhibiting minimal uptake of competing ions (Fig. 5(b)). The corresponding distribution coefficients (K_d) reveal a pronounced selectivity gap, with K_d (Au) on the order of 10^9 mL·g^{-1} and values for competing ions several orders of magnitude lower (Fig. 5(c)) [14]. This remarkable selectivity originates from the favorable interaction between nitrogen-containing active sites and Au species, combined with the *in situ* reduction of Au(III) to Au(0), which further drives gold enrichment. Recycling tests demonstrate that HNPC retains high Au removal efficiency over repeated adsorption–desorption cycles and can be effectively regenerated, enabling stable operation

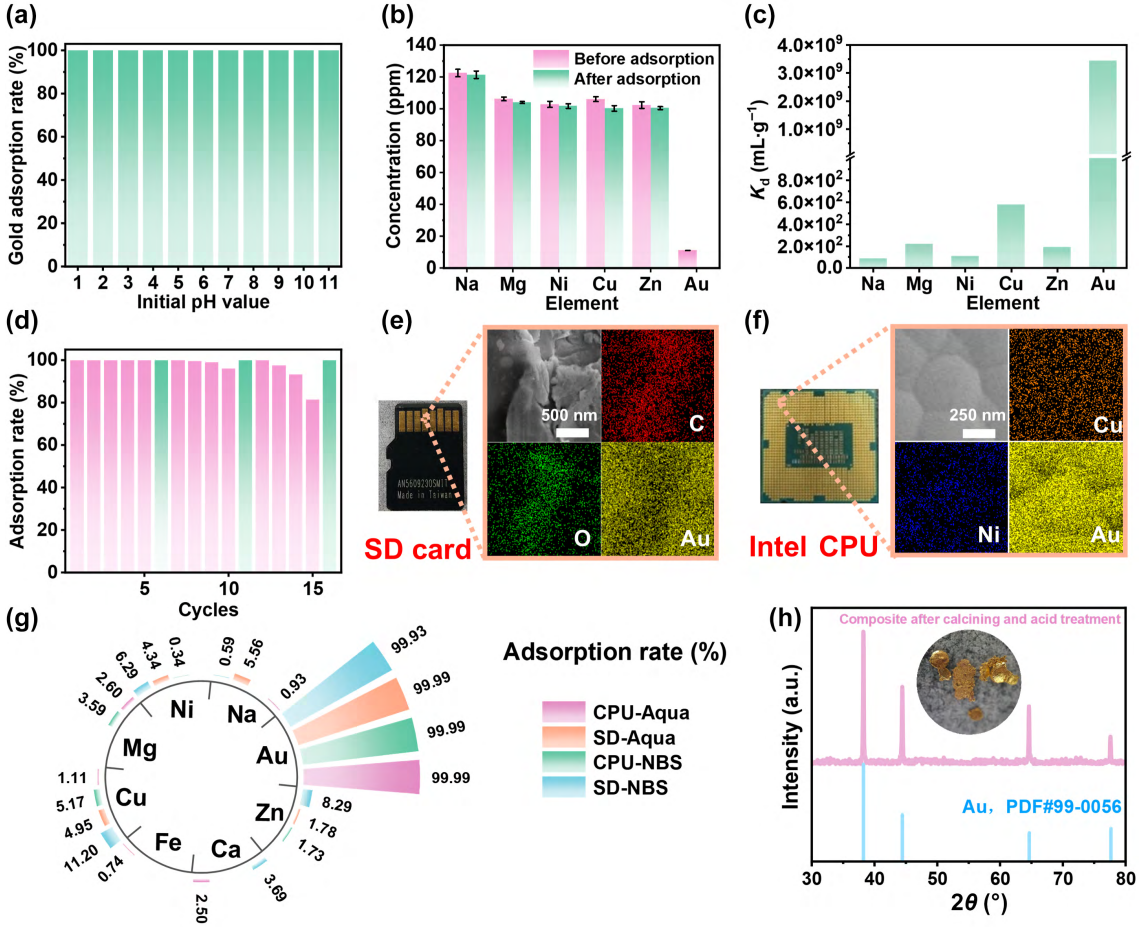

Figure 5 Robust and selective Au(III) extraction from complex matrices and real e–waste leachates. (a) Au(III) adsorption/removal efficiency of HNPC over a wide initial pH range (pH=1–11). (b) Selective adsorption in a competitive multicomponent solution: concentrations of coexisting ions (Na^+, Mg^{2+}, Ni^{2+}, Cu^{2+}, Zn^{2+}) and Au(III) before and after adsorption. (c) Distribution coefficients (K_d) for Au(III) and competing ions. (d) Recyclability test of HNPC over repeated adsorption cycles. SEM images and corresponding energy dispersive spectrometer (EDS) elemental maps from (e) SD card and (f) Intel CPU. (g) Elemental composition (inner ring) of diluted real leaching solution (CPU/SD; aqua regia vs. NBS/pyridine leaching) and the corresponding ion removal efficiencies by HNPC (color bar). (h) PXRD pattern of recovered gold product after calcination and acid treatment, compared with the standard Au reference (PDF#99–0056); inset shows the obtained metallic Au.

over 16 batches (Fig. 5(d); see the ESM, Recycling and Regeneration Tests). This durability benefits from the stable graphitized carbon framework and resilient nitrogen functionalities, which preserve structural integrity and maintain accessible adsorption sites during cyclic adsorption–desorption operation.

We then examined real leachates derived from SD cards and Intel CPUs. The compositions of the diluted leachates and the corresponding adsorption efficiencies are summarized in Fig. 5(g). SEM/EDS mapping confirms Au enrichment on HNPC after treatment with both types of leachate (Figs. 5(e) and 5(f)). ICP analysis before and after adsorption shows that HNPC selectively depletes Au even when major coexisting ions are present at hundreds of ppm, including a representative aqua-regia leachate containing only ~2.3 ppm Au (Fig. S20 in the ESM). The product obtained after calcination and acid washing exhibits diffraction peaks characteristic of metallic Au (Fig. 5(h)) and a purity of 99.68% by ICP-OES (Fig. S21 in the ESM), confirming that HNPC enables Au(III) capture-coupled reduction and recovery of metallic Au from chemically complex waste streams.

2.6 Catalytic reuse of recovered Au/HNPC for nitrate-to-ammonia electrocatalysis

Having established selective Au capture-to-reduction, we next examined whether the recovered Au/HNPC could be directly reused as a gas-diffusion-electrode catalyst for nitrate-to-ammonia electrocatalysis. Au/HNPC samples with different Au loadings were obtained by varying the Au(III) adsorption time (0.5 min, 1 h, and 24 h); for consistency, these catalysts are denoted HNPCs-0.5 min, HNPCs-1 h, and HNPCs-24 h, whereas pristine HNPC is denoted HNPCs. Nitrate electroreduction (eNO_3RR) was carried out in a gas-diffusion flow cell (Fig. 6(a)). NH_3 was quantified using a calibrated Nessler method, and NO_2^- was monitored by UV-Vis spectroscopy [62–64]. Among the series, HNPCs-1 h delivers the highest NH_3 selectivity, reaching a maximum NH_3 Faradaic efficiency (FE) of 96.6% at 200 mA·cm^{-2} (−0.705 V vs. RHE) with an NH_3 yield rate of 0.90 mmol·cm^{-2}·h^{-1}, while NO_2^- formation remains minor across the tested current-density range (Fig. 6(b), Fig. S22, and Table S6 in the ESM). Increasing current density boosts the NH_3 yield rate to 3.75 mmol·cm^{-2}·h^{-1} at 900 mA·cm^{-2} (Fig. 6(b) and Table S6 in the ESM). In contrast, pristine HNPCs and catalysts with insufficient or excessive Au loading (0.5 min and 24 h) show lower selectivity and/or productivity across the same current range (Figs. 6(c) and 6(d), Fig. S23, and Tables S6–S9 in the ESM), highlighting the importance of controlling Au nucleation and surface coverage on the hollow carbon scaffold.

Electrochemical diagnostics indicate that the superior

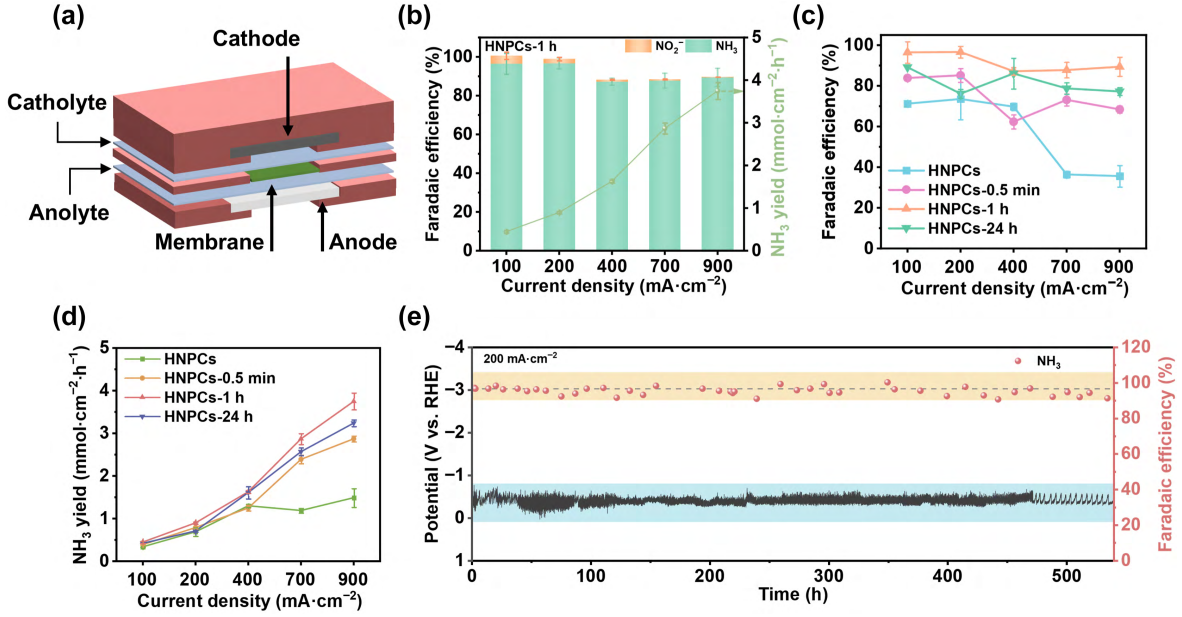

Figure 6 Upcycled Au/HNPC as an efficient and durable electrocatalyst for nitrate–to–ammonia conversion. (a) Schematic of the gas–diffusion flow cell configuration used for nitrate electroreduction, illustrating electrolyte flow, membrane separation, and electrode arrangement. (b) Faradaic efficiencies (FE) for NH_3 and NO_2^- yield rates of HNPCs–1 h toward eNO_3RR. (c) FEs, and (d) yield rates of HNPCs, HNPCs–0.5 min, HNPCs–1 h, and HNPCs–24 h at various applied current densities. (e) Long–term chronopotentiometry curve and NH_3 FEs of HNPCs–1 h at the current density of 200 mA·cm^{-2} over 535 h.

performance of HNPCs-1 h is associated with enhanced active-site accessibility and charge transport. HNPCs-1 h exhibits the largest double-layer capacitance (C_{dl} = 5.77 mF·cm^{-2}) derived from scan-rate-dependent cyclic voltammetry (Figs. S24 and S25 in the ESM) and the lowest charge-transfer resistance in electrochemical impedance spectroscopy (EIS) (Fig. S26 in the ESM), consistent with a higher electrochemically accessible surface area and faster interfacial electron transfer. During continuous operation at 200 mA·cm^{-2}, HNPCs-1 h maintains stable cell potential and periodically measured NH_3 FE values above 90% over 535 h (Fig. 6(e) and Table S10 in the ESM). Benchmarking against reported systems highlights the balanced selectivity, productivity, and durability of HNPCs-1 h under comparable flow-cell conditions (Fig. 1(c) and Table S11 in the ESM). Post-electrolysis SEM, PXRD, and XPS confirm that the catalyst morphology and Au valence state are largely preserved (Fig. S27 in the ESM), supporting stable confinement of Au domains on the conductive hollow N-doped carbon scaffold. Collectively, these results demonstrate that HNPC functions as a capture-to-catalyst materials platform, coupling selective Au recovery from e-waste leachates with electrocatalytic nitrate remediation.

3 Conclusion

We have developed a ZIF-8-derived hollow N-doped porous carbon that integrates selective gold recovery, *in situ* Au formation, and catalytic nitrate-to-ammonia conversion within one materials platform. The hollow mesoporous architecture accelerates ion transport and improves access to internal adsorption sites, whereas graphitic-N-associated sites provide a favorable interfacial environment for $AuCl_4^-$ adsorption and Au(III)-to-Au(0) reduction. This thermodynamic–kinetic co-design enables high-capacity and highly selective Au recovery under trace-target and strong-competition conditions, while retaining robust performance across a broad pH range and in real e-waste leachates. Combined time-resolved microscopy and spectroscopy, finite-element simulations, and DFT calculations support a mechanism in which hollow-structure-enabled transport and graphitic-N-regulated reactivity operate together during Au capture-to-reduction. The Au formed *in situ* on HNPC can be directly reused as a gas-diffusion-electrode catalyst for nitrate-to-ammonia conversion, linking precious-metal recovery with catalytic nitrogen remediation in a closed-loop route. These findings establish a capture-to-catalyst materials strategy for designing reactive porous carbons that integrate selective capture, interfacial transformation, and downstream valorization in complex aqueous waste streams.

4 Experimental section

4.1 Synthesis of HNPC and NPC

ZIF–8 nanocrystals were synthesized from $Zn(NO_3)_2{\cdot}6H_2O$ and 2-methylimidazole in methanol. A hollow precursor (HZIF–8) was then generated by tannic-acid etching of ZIF–8 in a methanol/water mixture. HZIF–8 was carbonized under flowing N_2 (50 sccm; 3 °C·min^{-1}; 2 h) at 700–1000 °C to yield HNPC-X, where X denotes the carbonization temperature; unless otherwise stated, HNPC refers to HNPC-900. The solid control (NPC) was prepared by carbonizing pristine ZIF–8 under otherwise identical conditions. Full synthetic procedures, precursor ratios and purification details are provided in the ESM.

4.2 Au(III) adsorption and gold recovery

Au(III) adsorption isotherms were measured by dispersing 5 mg of adsorbent in 10 mL $KAuCl_4$ solutions with initial Au concentrations ranging from 1 to 4000 mg·L^{-1} at pH ≈ 4 for 24 h. Kinetic experiments were performed using 5 mg of adsorbent in 200 mL of 100 mg·L^{-1} Au(III), and pH-dependent uptake, competitive adsorption, recycling and real-leachate recovery were evaluated under the conditions described in the ESM. Competitive solutions contained 10 ppm Au(III) and 100 ppm each of Na^+, Mg^{2+}, Ni^{2+}, Cu^{2+} and Zn^{2+}. CPU and SD-card leachates were

prepared by NBS/pyridine or aqua regia leaching followed by dilution before adsorption. Residual Au and competing ions were quantified by ICP-OES and ICP-MS. Adsorption equations and fitting procedures are given in the ESM.

4.3 Characterization and modeling

Morphology, pore structure and surface chemistry were analyzed by SEM, TEM/HAADF-STEM-EDS, PXRD, XPS, Raman spectroscopy, N_2 sorption and zeta-potential measurements, and the evolution of Au coordination was probed by Au L_3-edge XANES/EXAFS. Ion-transport behavior was simulated in COMSOL using hollow and solid hexagonal particle models with identical outer dimensions. Electronic-structure calculations were carried out in ORCA, with geometry optimization at the B97-3c level and single-point energies evaluated at the RI-B3LYP-D3(BJ)/def2-TZVP level. Charge and electrostatic-potential analyses were performed using Multiwfn and VMD. Instrument settings, fitting procedures and simulation parameters are provided in the ESM.

4.4 Electrocatalytic nitrate reduction

Au/HNPC catalysts with different Au loadings were obtained by varying the Au(III) adsorption time (0.5 min, 1 h and 24 h). Catalyst inks were prepared from 25 mg catalyst, n-propanol, a MWCNT suspension and Nafion, and were drop-cast onto Sigracet 29 BC carbon paper to afford gas-diffusion electrodes with a catalyst loading of 0.5 mg·cm^{-2}. Nitrate electroreduction was conducted in an acrylic flow cell (channel size 2 cm × 0.5 cm × 0.15 cm; exposed cathode area 1 cm^2) using 1 M KOH as the anolyte and 1 M KOH + 0.5 M KNO_3 as the catholyte, with Ag/AgCl and Ni foam as the reference and counter electrodes, respectively. NH_3 and NO_2^- concentrations were quantified using Nessler and Griess assays, respectively, and C_{dl} was estimated from scan-rate-dependent cyclic voltammetry in 0.1 M $HClO_4$. Detailed electrode preparation, calibration procedures and product analysis are described in the ESM.

Acknowledgements

The authors acknowledge financial support from the National Natural Science Foundation of China (Nos. 52473050, 22275166, 22579130, and 52572111), the Zhoushan Key and Generic Technology Research Program (No. 2025C03001) and the Natural Science Foundation of Zhejiang Province (No. QK26E020001). The authors also thank the Analysis and Testing Center at Zhejiang University of Technology for assistance with characterization.

Author contributions

T.K., W.L., J.-J.L., and G.M. conceived and supervised the study. Y.D., R.G., W.D., and Z.-J.W. synthesized the materials, performed characterization and electrochemical experiments, and analyzed the data. R.G., Z.-J.W., and G.M. performed the computational modeling and theoretical analysis. Y.D., R.G., W.L., and T.K. drafted the manuscript. All authors discussed the results and revised the manuscript.

Declaration of conflicting interests

The authors declare no conflicting interests regarding the content of this article.

Data availability

All data needed to support the conclusions in the paper are presented in the manuscript and/or the Supplementary Materials. Additional data related to this paper may be requested from the corresponding author upon request.

Electronic Supplementary Material: Supplementary material (detailed experimental procedures for HNPC synthesis and characterization, gold recovery, computational simulations, and nitrate-to-ammonia electrocatalysis) is available in the online version of this article at https://doi.org/10.26599/NRE.2026.9120261.

References

[1] Tourchi Moghadam, M. T.; Kang, K. Recent advances in biomass-derived carbon materials-emerging strategies for dual applications in precious metal recovery and energy storage. *J. Mater. Sci.* **2026**, *61*, 5611–5644.

[2] Li, H.; Huang, X. H. Synergistic dual-mechanism design: NiO-decorated pyrrolic-N doped carbon for ultrahigh-rate and selective recovery of silver ions via capacitive deionization. *Desalination* **2026**, *625*, 119916.

[3] Su, L. X.; Cui, C. X.; Yu, H. J.; Lu, Y. L.; Cheng, J. B.; Wu, L. Q.; Li, W. T.; Luo, W.; Pang, H. pH-dependent behavior of Ru-based hydrogen-oxidation electrocatalysis by a reconstructed hydrogen-bond network. *Angew. Chem., Int. Ed.* **2026**, *65*, e8831785.

[4] Lu, H. T.; Liu, Y. X.; Qi, Y. L.; Zhou, Y. F.; Yang, Z. B.; Pang, H. Zebra-inspired radiative modulator for climate-customized thermal management enabled by metal-organic framework. *Sci. China Mater.* **2026**, *69*, 1006–1013.

[5] Zhang, Z. Chen-Ning Yang: A legacy of sustainable scientific development and global cooperation. *Sustain. Eng. Novit* **2025**, *1*, 8.

[6] Liu, Y.; Yuan, Y. W.; Wang, R.; Duan, L. H.; Lv, R. G.; Chang, Y. N.; Wu, H. Y.; Yan, X. L.; Xing, R.; Holze, R. Computational studies for aqueous zinc-ion secondary batteries. *Sustain. Eng. Novit* **2025**, *1*, 6.

[7] Gao, Y.; Ye, C. G.; Wang, R.; Li, W. T.; Pang, H. Hybrid and flow-electrode capacitive deionization: Materials design, multispecies removal, and smart regulation. *Sustain. Eng. Novit* **2025**, *1*, 7.

[8] Zadehnazari, A.; Auras, F.; Altaf, A. A.; Zarei, A.; Khosropour, A.; Amirjalayer, S.; Abbaspourrad, A. Recycling e-waste into gold-loaded covalent organic framework catalysts for terminal alkyne carboxylation. *Nat. Commun.* **2024**, *15*, 10846.

[9] Amato, A.; Beolchini, F. Turning e-waste into opportunity. *Nat. Rev. Electr. Eng.* **2024**, *1*, 212–213.

[10] Hagelüken, C.; Corti, C. W. Recycling of gold from electronics: Cost-effective use through 'Design for Recycling'. *Gold Bull.* **2010**, *43*, 209–220.

[11] Shangguan, Y. Z.; Gu, X. S.; Yang, S. H.; Feng, X. Z.; Hu, Q. S.; Chen, X. H.; Chen, H. Edge-engineered interfacial carrier dynamics for efficient photocatalytic gold recovery. *Angew. Chem., Int. Ed.* **2026**, *65*, e7275462.

[12] Zhu, S. S.; Jin, Y. C.; Hou, Y. X.; Li, J. H.; Meng, X. X.; Li, Z. P.; Liu, X. M. Hexamethoxy triazocoronene based covalent organic frameworks: A family of tailored tools for efficient gold recovery. *Angew. Chem., Int. Ed.* **2026**, *65*, e4681230.

[13] Li, F.; Zhu, J. Y.; Sun, P. Z.; Zhang, M. R.; Li, Z. Q.; Xu, D. X.; Gong, X. Y.; Zou, X. L.; Geim, A. K.; Su, Y. et al. Highly efficient and selective extraction of gold by reduced graphene oxide. *Nat. Commun.* **2022**, *13*, 4472.

[14] Xue, T. W.; He, T.; Peng, L.; Syzgantseva, O. A.; Li, R. Q.; Liu, C. B.; Sun, D. T.; Xu, G. K.; Qiu, R. X.; Wang, Y. L. et al. A customized MOF-polymer composite for rapid gold extraction from water matrices. *Sci. Adv.* **2023**, *9*, eadg4923.

[15] Fu, K. X.; Liu, X.; Zhang, X. L.; Zhou, S. Q.; Zhu, N. W.; Pei, Y.;

Luo, J. M. Utilizing cost-effective pyrocarbon for highly efficient gold retrieval from e-waste leachate. *Nat. Commun.* **2024**, *15*, 6137.
[16] Yan, P. Y.; Zhao, W.; McBride, F.; Cai, D. N.; Dale, J.; Hanna, V.; Hasell, T. Mechanochemical synthesis of inverse vulcanized polymers. *Nat. Commun.* **2022**, *13*, 4824.
[17] Huang, T. F.; Lin, K. J.; Zhuang, Y. R.; Sun, Y. E.; Lin, W. C.; Li, C. H.; Lin, C. C.; Chang, E. C.; Chang, C. L.; Liu, Y. C. et al. Flexible, nonfused sulfone functionalized polymer with enhanced active site access for photocatalytic sacrificial hydrogen evolution. *Sci. Adv.* **2025**, *11*, eadx1629.
[18] Shin, K. Y.; Hong, J. Y.; Jang, J. Heavy metal ion adsorption behavior in nitrogen-doped magnetic carbon nanoparticles: Isotherms and kinetic study. *J. Hazard. Mater.* **2011**, *190*, 36–44.
[19] Yang, J.; Xu, M.; Wang, J. Y.; Jin, S. B.; Tan, B. E. A facile approach to prepare multiple heteroatom-doped carbon materials from imine-linked porous organic polymers. *Sci. Rep.* **2018**, *8*, 4200.
[20] Lan, Y.; Xu, S.; Fu, Y. H.; Jin, L.; Han, Y. B.; He, X.; Wang, Q. L.; Lv, Y.; Cui, H. S. The selective adsorption mechanism of heteroatom-doped carbon nanotubes for heavy metals in wastewater. A DFT study. *Diam. Relat. Mater.* **2025**, *152*, 111875.
[21] Zhang, W.; Li, H.; Feng, D. M.; Wu, C. L.; Sun, C. H.; Jia, B. H.; Liu, X.; Ma, T. Y. MOF-derived 1D/3D N-doped porous carbon for spatially confined electrochemical CO_2 reduction to adjustable syngas. *Carbon Energy* **2024**, *6*, e461.
[22] Gao, M. B.; Li, H.; Yang, M.; Gao, S. S.; Wu, P. F.; Tian, P.; Xu, S. T.; Ye, M.; Liu, Z. M. Direct quantification of surface barriers for mass transfer in nanoporous crystalline materials. *Commun. Chem.* **2019**, *2*, 43.
[23] Brandani, S.; Hwang, S.; Kärger, J.; Mangano, E. Diffusion anomaly in nanopores as a rich field for theorists and a challenge for experimentalists. *Nat. Commun.* **2024**, *15*, 5721.
[24] Schneider, D.; Mehlhorn, D.; Zeigermann, P.; Kärger, J.; Valiullin, R. Transport properties of hierarchical micro-mesoporous materials. *Chem. Soc. Rev.* **2016**, *45*, 3439–3467.
[25] Coasne, B.; Galarneau, A.; Gerardin, C.; Fajula, F.; Villemot, F. Molecular simulation of adsorption and transport in hierarchical porous materials. *Langmuir* **2013**, *29*, 7864–7875.
[26] Goswami, N.; Rao, S.; Abad, S. D.; Ruba, A.; Thakkar, H.; Mukherjee, P. P.; Singh, R. P.; Spendelow, J. S.; Holby, E. F.; Zelenay, P. et al. Role of hierarchical porosity in dictating adsorption dynamics in direct air capture systems. *ACS Appl. Energy Mater.* **2025**, *8*, 11758–11770.
[27] Li, X. H.; Wang, Y. L.; Wen, J.; Zheng, L. L.; Qian, C.; Cheng, Z. H.; Zuo, H. Y.; Yu, M. Q.; Yuan, J. Y.; Li, R. et al. Porous organic polycarbene nanotrap for efficient and selective gold stripping from electronic waste. *Nat. Commun.* **2023**, *14*, 263.
[28] Luo, J.; Luo, X.; Xie, M.; Li, H. Z.; Duan, H. Y.; Zhou, H. G.; Wei, R. J.; Ning, G. H.; Li, D. Selective and rapid extraction of trace amount of gold from complex liquids with silver(I)-organic frameworks. *Nat. Commun.* **2022**, *13*, 7771.
[29] Uehara, A.; Chang, S. Y.; Booth, S. G.; Schroeder, S. L. M.; Mosselmans, J. F. W.; Dryfe, R. A. W. Redox and ligand exchange during the reaction of tetrachloroaurate with hexacyanoferrate(II) at a liquid-liquid interface: Voltammetry and X-ray absorption fine-structure studies. *Electrochim. Acta* **2016**, *190*, 997–1006.
[30] Wu, Y. Y.; Guo, Y. Y.; Xue, T. W.; Shao, Z. Y.; Xu, L. Z.; Kuang, J. H.; Li, R. Q.; Xu, G. K.; Chen, P.; Hao, W. L. et al. Light-promoted efficient gold recovery enabled by a polydopamine-functionalized covalent organic framework. *Angew. Chem., Int. Ed.* **2026**, *65*, e26042.
[31] Yang, Q. Q.; Li, S. X.; Han, J. Y.; Chen, M. W.; Zhao, W. K.; Wang, S.; Rodriguez, R. D.; Zhang, T. Engineering heteroatomic nanotraps in vinyl-benzazole COFs: Record capacity and 99% selectivity for photocatalytic gold recovery from E-waste. *Adv. Mater.* **2026**, *38*, e72446.
[32] Wu, Y. H.; Luo, J. X.; Wang, S. X.; Zhu, R.; Ye, J. Q.; Yang, X. R.; Tang, X. N.; Luo, G. W. Chitosan-interpenetrated metal organic framework for targeted recovery of gold from gold-electroplating wastewater. *Water Res.* **2026**, *288*, 124736.
[33] Qin, J. L.; Liu, H. Z.; Fang, Z. Y.; Pei, J. J.; Yin, K.; Fu, K. X.; Luo, J. M. Selective gold extraction from e-waste leachate via sulfur-redox mechanisms using sulfhydryl-functionalized MOFs. *Water Res.* **2025**, *275*, 123170.
[34] Yang, Z. B.; Lu, H. T.; Li, Q.; Guo, X. T.; Li, Q.; Zhou, H. J.; Wang, B. X.; Qi, Y. L.; Chen, H. C.; Yang, M. F. et al. Nano/micro metal-organic framework-derived ceramics for sustainable energy saving/capturing. *Adv. Mater.* **2026**, *38*, e12289.
[35] Shao, Q. S.; Ding, Y. T.; Liu, W. X.; Guan, J.; Meng, G.; Kuang, T. R.; Wang, D. S. Bandgap engineering on UiO-66 metal-organic framework derivatives for solar-driven seawater desalination. *Adv. Sci.* **2025**, *12*, 2502989.
[36] Kuang, T. R.; Deng, L. B.; Liu, M. J.; Ding, Y. T.; Guo, W.; Cai, Z.; Liu, W. X.; Huang, Z. X. Facet engineering of metal-organic frameworks for triboelectric nanogenerators-based self-powered water splitting. *Adv. Mater.* **2025**, *37*, 2415616.
[37] Zhang, W.; Jiang, X. F.; Zhao, Y. Y.; Carné-Sánchez, A.; Malgras, V.; Kim, J.; Kim, J. H.; Wang, S. B.; Liu, J.; Jiang, J. S. et al. Hollow carbon nanobubbles: Monocrystalline MOF nanobubbles and their pyrolysis. *Chem. Sci.* **2017**, *8*, 3538–3546.
[38] Wang, J. L.; Guo, X. Rethinking of the intraparticle diffusion adsorption kinetics model: Interpretation, solving methods and applications. *Chemosphere* **2022**, *309*, 136732.
[39] Liu, Y. New insights into pseudo-second-order kinetic equation for adsorption. *Colloids Surf. A: Physicochem. Eng. Asp.* **2008**, *320*, 275–278.
[40] Palma, G.; Demanet, R.; Jorquera, M.; Mora, M. L.; Briceño, G.; Violante, A. Effect of pH on sorption kinetic process of acidic herbicides in a volcanic soil. *J. Soil Sci. Plant Nutr.* **2015**, *15*, 549–560.
[41] Li, J. J.; Xia, W.; Xu, X. T.; Jiang, D.; Cai, Z. X.; Tang, J.; Guo, Y. N.; Huang, X. L.; Wang, T.; He, J. P. et al. Selective etching of metal-organic frameworks for open porous structures: Mass-efficient catalysts with enhanced oxygen reduction reaction for fuel cells. *J. Am. Chem. Soc.* **2023**, *145*, 27262–27272.
[42] Lim, K. R. G.; Aizenberg, M.; Aizenberg, J. Colloidal templating in catalyst design for thermocatalysis. *J. Am. Chem. Soc.* **2024**, *146*, 22103–22121.
[43] Tian, Q.; Jing, L. Y.; Du, H. N.; Yin, Y. C.; Cheng, X. L.; Xu, J. X.; Chen, J. Y.; Liu, Z. X.; Wan, J. Y.; Liu, J. et al. Mesoporous carbon spheres with programmable interiors as efficient nanoreactors for H_2O_2 electrosynthesis. *Nat. Commun.* **2024**, *15*, 983.
[44] Xue, C.; Zhou, X. R.; Li, X. H.; Yang, N.; Xin, X.; Wang, Y. S.; Zhang, W. N.; Wu, J. S.; Liu, W. J.; Huo, F. W. Rational synthesis and regulation of hollow structural materials for electrocatalytic nitrogen reduction reaction. *Adv. Sci.* **2022**, *9*, 2104183.
[45] Zhang, W. D.; Zhao, H.; Liu, Y.; Gu, Z. G. Open hollow metal-organic frameworks: Synthesis strategies, applications and challenges. *Coord. Chem. Rev.* **2025**, *541*, 216829.
[46] Sun, Y. F.; Cao, Y. Q.; Wang, L. L.; Mu, X. T.; Zhao, Q. F.; Si, R.; Zhu, X. J.; Chen, S. J.; Zhang, B. S.; Chen, D. et al. Gold catalysts containing interstitial carbon atoms boost hydrogenation activity. *Nat. Commun.* **2020**, *11*, 4600.
[47] Imbir, G.; Wach, A.; Czapla-Masztafiak, J.; Wójcik, A.; Sá, J.; Szlachetko, J. Probing electronic-structure pH-dependency of Au nanoparticles through X-ray absorption spectroscopy. *Sci. Rep.* **2024**, *14*, 30059.
[48] Harada, M.; Kizaki, S. Formation mechanism of gold nanoparticles synthesized by photoreduction in aqueous ethanol solutions of polymers using *in situ* quick scanning X-ray absorption fine structure and small-angle X-ray scattering. *Cryst. Growth Des.* **2016**, *16*, 1200–1212.
[49] Uehara, A.; Booth, S. G.; Chang, S. Y.; Schroeder, S. L. M.; Imai, T.; Hashimoto, T.; Mosselmans, J. F. W.; Dryfe, R. A. W. Electrochemical insight into the Brust-Schiffrin synthesis of Au nanoparticles. *J. Am. Chem. Soc.* **2015**, *137*, 15135–15144.
[50] Kömür, A. İ.; Kızıl, Ç.; Karaman, C. Nature's blueprint for energy:

Biomass-derived heteroatom-doped graphene materials for advanced energy applications. *Carbon Lett.* **2025**, *35*, 919–961.
[51] Duff, D. G.; Ross, S. M. C.; Vaughan, D. H. Adsorption from solution: An experiment to illustrate the Langmuir adsorption isotherm. *J. Chem. Educ.* **1988**, *65*, 815.
[52] Malhotra, M.; Puglia, M.; Kalluri, A.; Chowdhury, D.; Kumar, C. V. Adsorption of metal ions on graphene sheet for applications in environmental sensing and wastewater treatment. *Sens. Actuators Rep.* **2022**, *4*, 100077.
[53] Nguyen, V. T.; Fitzgerald, M. A.; Ibbotson, D.; Foster, J.; Dzara, M. J.; Zaccarine, S. F.; Vyas, S.; Pylypenko, S. Effects of graphitic and pyridinic nitrogen defects on transition metal nucleation and nanoparticle formation on N-doped carbon supports: Implications for catalysis. *ACS Appl. Nano Mater.* **2022**, *5*, 14922–14933.
[54] Xie, X. Q.; Long, J. L.; Xu, J.; Chen, L. M.; Wang, Y.; Zhang, Z. Z.; Wang, X. X. Nitrogen-doped graphene stabilized gold nanoparticles for aerobic selective oxidation of benzylic alcohols. *RSC Adv.* **2012**, *2*, 12438.
[55] Ayiania, M.; Hensley, A. J. R.; Groden, K.; Garcia-Perez, M.; McEwen, J. S. Thermodynamic stability of nitrogen functionalities and defects in graphene and graphene nanoribbons from first principles. *Carbon* **2019**, *152*, 715–726.
[56] Zhou, L.; Zhu, H. D.; Zeng, W. Density functional theory study on the adsorption mechanism of sulphide gas molecules on α-Fe_2O_3(001) surface. *Inorganics* **2021**, *9*, 80.
[57] Mohammadi, M.; Alirezapour, F.; Khanmohammadi, A. Adsorption of transition metal cations (Cr^{2+}, Mn^{2+}, Fe^{2+}, Cu^{+}, Ag^{+} and Au^{+}) on boron nitride nanotube: Structural analysis and electronic properties. *Adv. J. Chem., Sect. A* **2024**, *7*, 355–373.
[58] Laeber, K. F. P.; Prates, L. M.; Baptista, L.; Cruz, M. T. M. Study of the electronic structure of coronene doped with nitrogen atoms and its effect on CO_2 capture. *ACS Omega* **2025**, *10*, 16559–16578.
[59] Ju, W.; Bagger, A.; Hao, G. P.; Varela, A. S.; Sinev, I.; Bon, V.; Roldan Cuenya, B.; Kaskel, S.; Rossmeisl, J.; Strasser, P. Understanding activity and selectivity of metal-nitrogen-doped carbon catalysts for electrochemical reduction of CO_2. *Nat. Commun.* **2017**, *8*, 944.
[60] Meng, Y.; Ying, L. B.; Tao, Y. N.; Ma, L.; Li, B. N.; Xing, Y.; Liu, X. Y.; Ma, Y. J.; Wen, X. D. DFT study on effect of metal type and coordination environment on CO_2 ECR to C1 products over M–N–C catalysts. *Langmuir* **2024**, *40*, 10663–10675.
[61] Cao, J. Z.; Xu, Z. M.; Chen, Y.; Li, S. J.; Jiang, Y.; Bai, L. L.; Yu, H.; Li, H. X.; Bian, Z. F. Tailoring the Asymmetric Structure of NH_2–UiO-66 metal-organic frameworks for light-promoted selective and efficient gold extraction and separation. *Angew. Chem., Int. Ed.* **2023**, *62*, e202302202.
[62] Zhou, L. M.; Chen, X. Q.; Zhu, S. J.; You, K.; Wang, Z. J.; Fan, R.; Li, J.; Yuan, Y. F.; Wang, X.; Wang, J. C. et al. Two-dimensional Cu plates with steady fluid fields for high-rate nitrate electroreduction to ammonia and efficient Zn-nitrate batteries. *Angew. Chem., Int. Ed.* **2024**, *63*, e202401924.
[63] Yang, M. S.; Chen, M. Y.; Wang, Y. Q.; Ma, J. J.; Zhang, L.; Hu, C. J.; Zhuo, L. C.; Feng, Y. H.; Liu, X. J. Dual-function FeCo bimetallic nanoclusters for ammonia electrosynthesis from nitrate/nitrite reduction. *Commun. Chem.* **2025**, *8*, 267.
[64] Wang, Z. W.; Chen, M. Y.; Lu, G. L.; Xu, J. B.; Zhuo, L. C.; Wu, Y. H.; Liu, X. J. Single-atom catalysts toward electrocatalytic urea synthesis via C–N coupling reactions. *Chem. Commun.* **2025**, *61*, 13601–13615.

Yutong Ding received his Ph.D. degree in Zhejiang University of Technology. He is currently a Postdoctoral Researcher at the College of Materials Science and Engineering, Zhejiang University of Technology. His research focuses on the design and development of functional materials and their applications.

Ruicong Geng received his Master's degree from Zhejiang University of Technology. He is currently employed at Hangzhou Xingchuan Novel Material Technology Co., Ltd. His research focuses on the design of porous carbon and gold recovery.

Jing-Jing Lv received her Ph.D. degree from Nanjing University. She is currently a Full Professor at the College of Chemistry and Materials Engineering, Wenzhou University. Her research focuses on electrocatalytic energy conversion.

Ge Meng received his Ph.D. degree from Beijing University of Chemical Technology. He is currently an Associate Research Professor at the College of Chemistry and Materials Engineering, Wenzhou University. His research focuses on the development of functional nanomaterials and their applications in heterogeneous catalysis and electrocatalysis.

Wenxian Liu received his Ph.D. degree from Beijing University of Chemical Technology. He is currently an Associate Professor at the College of Materials Science and Engineering, Zhejiang University of Technology. His research focuses on electrocatalysis and aqueous zinc-based batteries.

Tairong Kuang received his Ph.D. degree from South China University of Technology and is currently a Full Professor at the College of Materials Science and Engineering, Zhejiang University of Technology. His research focuses on the design and development of advanced functional materials, including functional polymers, polymer composites, porous carbon materials, and nanostructured materials for energy, environmental, and emerging applications.